Embeddings of a strange attractor into $\mathbb{R}^3$

Tsvetelin D. Tsankov, Arunasri Nishtala and Robert Gilmore
Physics Department, Drexel University, Philadelphia, Pennsylvania 19104, USA

(Dated: January 22, 2004, *Physical Review E*: To be submitted.)

The algorithm for determining a global Poincaré section is applied to a previously studied dynamical system on $\mathbb{R}^2 \times \mathbb{S}^1$ and a one-parameter family of embeddings of the strange attractor it generates into $\mathbb{R}^3$. We find that the topological properties of the attractor are embedding-dependent to a limited extent. These embeddings rigidly preserve mechanism, which is a simple stretch and fold. The embeddings studied show three discrete topological degrees of freedom: parity; global torsion; and braid type of the genus-one torus bounding the embedded attractor.

I. INTRODUCTION

Embeddings are the primary tool used by experimentalists to study scalar time series generated by chaotic dynamical systems. A number of embedding theorems guarantee that data generated by an n-dimensional dynamical system can be used to recreate the dynamics of that system in a space of sufficiently high dimension [1, 2]. However, these theorems are silent on a number of points - in particular, on how the geometry of an attractor depends on the embedding.

In order to address this question, Mindlin and Solari studied a one-parameter family of mappings into $\mathbb{R}^3$ [3]. In particular, they mapped chaotic scalar time series generated by a dynamical system that had been found to represent a fluid experiment fairly accurately [4, 5]. They found two ranges of parameter values in which embeddings existed, separated by a range of parameter values at which self-intersections occurred. They reached two conclusions that might create problems for the applications of topological analyses to data. The first is that applying the traditional algorithm for choosing a Poincaré section creates subtleties in constructing and understanding braids in the attractor. This presents a problem because chaotic data sets have been identified principally by the braids (unstable periodic orbits and their links) that they contain. The second is that the topological properties of a strange attractor are not invariant under embeddings. In particular, they found that the same orbit, in two different embeddings, appeared to have different topological entropies. This presents a problem because topological entropy is embedding-independent [6].

Recent advances in our understanding of the structure of chaos in three dimensions [7, 8] enable us to return to the problem and provide a more positive answer to the embedding question. There is now an algorithm for properly constructing all the components of a Poincaré section in any dissipative dynamical system with Lyapunov dimension $d_L < 3$ [7, 8]. With such a choice, constructing and interpreting braids is algorithmic. We also find, in agreement with Mindlin and Solari, that the topological structure is not embedding independent. However, we find that there are only three degrees of freedom that are available to change the topological structure of a strange attractor with embedding: parity; global torsion; and braid type of the torus bounding the embedded attractor.

This work is organized as follows. In Sect. II we introduce the dynamical system used for this and the previous study of embeddings. We show that chaos is generated by a simple Smale horseshoe (stretch and fold) mechanism. In Sect. III we describe the topological properties of this attractor in the natural phase space, which is the solid torus $\mathbb{R}^2 \times \mathbb{S}^1$. These properties are unchanged under the preferred embedding of $\mathbb{R}^2 \times \mathbb{S}^1$ in $\mathbb{R}^3$. The one-parameter family of embeddings into $\mathbb{R}^3$ that was studied in [3] is introduced in Sect. IV. In Sect. V we apply the new algorithm for choosing a global Poincaré section [7, 8] and discuss how this is related to intersections of the embedded attractor with the plane $\dot{X} = 0$. Proper choice of the global Poincaré section positively resolves the braid problem. In Sect. VI we describe extrinsic embeddings obtained with three different choices of the delay parameter. Between parameter values at which embeddings occur are values at which self-intersections occur. An algorithm for determining self-intersections is presented in Sect. VII. In this section we also describe how the extrinsic topology of the embedding changes on passing through self-intersections. We summarize our findings in the closing section. These findings are: (1) there is an algorithm for constructing the components of a Poincaré section for any embedding. When applied, construction of braids is algorithmic. (2) The topological properties of the strange attractor can vary from one embedding to another. However, the only ways they can differ in the class of embeddings studied are: the handedness of the folding; the global torsion; the braid type of the period-one orbit guiding the bounding torus.

II. DYNAMICAL SYSTEM AND PHASE SPACE

The equations used in [3] as a vehicle to study the properties of embeddings are

$$\begin{aligned} \dot{X} &= Y \\ \dot{Y} &= \mu f(\phi) X + \nu f(\phi) Y - X^3 + X^2 Y \\ \dot{\phi} &= \omega \end{aligned} \tag{1}$$

where $f(\phi) = [1 + \epsilon \cos(\phi)]$. This set of equations describes a periodically forced Takens-Bogdanov scenario. They have been used successfully to model the behavior of a fluid heated from below [4]. As a result, we treat the time series $X(t)$, or $X(i)$, the way we would treat experimental data.

The equations (1) were integrated with a standard RK4 integrator with time step sizes $\delta t = 10^{-3}T$ and $T/2^k$, $k = 10$, where T is the period of the external forcing, $T = 2\pi/\omega$. The equations were studied at control parameter values $\mu = 1.0434$, $\nu = -1.0$, $\epsilon = 0.45$, $\omega = 0.399$. For these values of the control parameters the system (1) generates two disconnected strange attractors. Only one of these is shown in the X-Y projection in Fig. 1. The other strange attractor is obtained by inversion: $(X, Y) \to (-X, -Y)$. For slightly larger value, $\nu = -0.9 \times \mu$, there is a symmetry-restoring bifurcation leading to a strange attractor with inversion symmetry: $(X, Y) \to (-X, -Y)$.

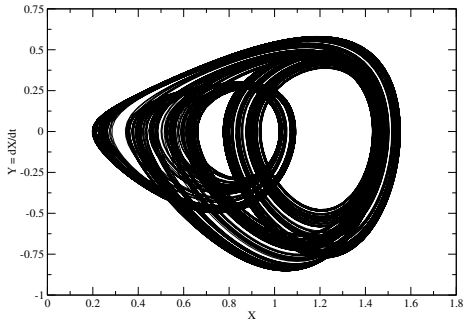

FIG. 1: A strange attractor generated by Eq(1) is plotted in the $X, \dot{X}$ plane. Another attractor is obtained from a change in initial conditions: $(X, Y) \to (-X, -Y)$. Parameter values: $\mu = 1.0434$, $\nu = -1.0$, $\epsilon = 0.45$, $\omega = 0.399$.

The phase space for the dynamical system (1) is $\mathbb{R}^2 \times \mathbb{S}^1$. Any stroboscopic section $\phi =$ constant can be chosen as a Poincaré section in this phase space. The intersection of the strange attractor with the section $\phi = 0$ is shown in Fig. 2. A first return map of this section to itself was constructed and is shown in Fig. 3. The coordinate used to construct this return map is the arc length measured along an approximation to the intersection shown in Fig. 2. The return map shows that the strange attractor is described by a branched manifold with two branches [9–12]. Unstable orbits of periods 1, 2, 4, and 5 were located by the method of close returns on the scalar time series $X(t)$, and by the method of close returns on the intersection shown in Fig. 2. These orbits were used for topological analyses. The period one and period two orbits are shown in Fig. 4. This figure shows the $X(t)$ value along these two orbits for two full driving periods.

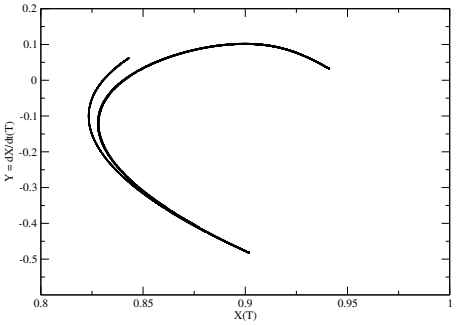

FIG. 2: Intersection of the strange attractor with a stroboscopic section (Poincaré section) at $\phi = 0.0$.

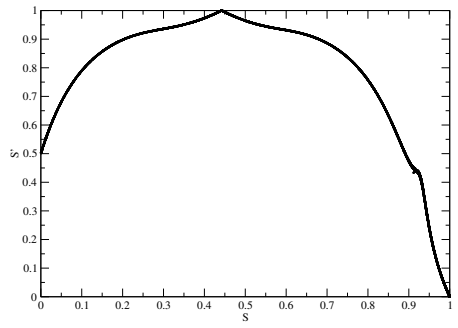

FIG. 3: Return map for the stroboscopic section (Fig. 2) onto itself. The parameter s is related to the arc length along the intersection of the attractor with the plane $\phi = 0$.

III. INTRINSIC STRUCTURE AND PREFERRED EMBEDDINGS

The phase space for the dynamical system (1) is the *intrinsic* solid torus $\mathbb{R}^2 \times \mathbb{S}^1$. The structure of the attrac-

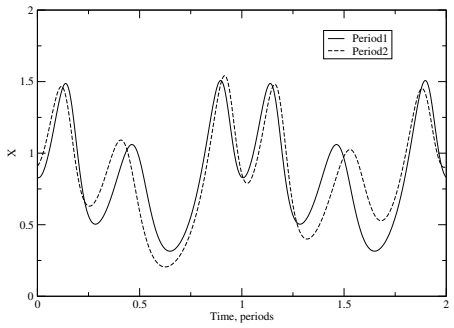

FIG. 4: Period-one and period-two orbits in the X-t plane.

tor in this phase space was determined by computing the relative rotation rates [13, 12] of the periods-one, -two, and -four orbits extracted from the data. For the period-one and period-two orbits this topological index can be determined by counting crossings in Fig. 4. For the embedding shown, with $Y = \dot{X}$ out of the plane, all crossings are left-handed. There are 10 (negative) crossings, so the linking number is -5 and the average number of rotations per period is $-5/2$.

The computation is simpler if we project the difference $\mathbf{X}_2(t) - \mathbf{X}_1(t)$ onto either the X-t plane (Fig. 5) or the X-Y plane (Fig. 6). In the first case it is sufficient to count the number of zero crossings. In the second case we count the number of times this difference rotates around the origin.

The relative rotation rates for the first three orbits in the period-doubling cascade are

RRR	1	2	4
1	-3	$\frac{1}{2}$	$\frac{1}{2}$
2	$\frac{1}{2}$	$-$	$\frac{1}{2}, \frac{1}{4}$
4	$\frac{1}{2}$	$\frac{1}{2}, \frac{1}{4}$	$-$

(2)

This shows that generation of chaos is due to a right-handed Smale horseshoe mechanism together with a global torsion of -3 [12, 13]. The right- and left-handed Smale horseshoe templates are described by the template and layering matrices [12]

	Right $-$ handed	Left $-$ handed
Template Matrix	$\begin{bmatrix} 0 & 0 \\ 0 & 1 \end{bmatrix}$	$\begin{bmatrix} 0 & 0 \\ 0 & -1 \end{bmatrix}$
Layering Matrix	$\begin{bmatrix} 0 & -1 \end{bmatrix}$	$\begin{bmatrix} 0 & 1 \end{bmatrix}$

These two branched manifolds are mirror images of each other. Linking numbers (and relative rotation rates) of all orbit pairs in the right handed Smale horseshoe with zero global torsion are positive or zero. Linking numbers of corresponding orbits in the left-handed Smale horseshoe are negatives of those in the right-handed Smale horseshoe. The topological organization of all orbits in the right-handed branched manifold is the mirror image of those in the left-handed branched manifold. The orbit forcing order [14], [15] in the horseshoe is independent of the handedness and the global torsion.

The global torsion -3 is compatible with estimates based on reasonable physical approximations. In driven systems the global torsion is slightly detuned from the ratio of the driving period to the intrinsic period: $T_{drive}/T_{intrinsic}$ (cf. Figs. 7.37 and 7.45 in [12]). The intrinsic period can be estimated by locating the nontrivial instantaneous fixed points at $(X, Y) = (\pm\sqrt{\mu f}, 0)$ and carrying out a stability analysis at these fixed points. A simple calculation gives $\omega_{intrinsic} \simeq \sqrt{2\mu f}$, so that $T_{drive}/T_{intrinsic} \simeq \sqrt{\frac{2\mu}{0.399}} \int_0^{2\pi} \sqrt{1 + \epsilon\cos(\phi)} \frac{d\phi}{2\pi} \simeq 3.57$.

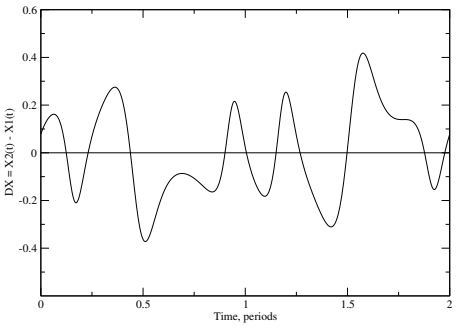

FIG. 5: Relative rotation rates for the period-one and period-two orbits. The difference $\mathbf{X}_2(t) - \mathbf{X}_1(t)$ is projected onto the X-t plane and the number of zero crossings is counted. The relative rotation rate is half the number of zero crossings divided by the period (2).

The intrinsic solid torus $\mathbb{R}^2 \times \mathbb{S}^1$ was embedded in $\mathbb{R}^3$ with a preferred framing [16]. This was done using

$$\begin{aligned} X_1(t) &= (a + X(t))\cos(\omega t) \\ X_2(t) &= (a + X(t))\sin(\omega t) \\ X_3(t) &= Y(t) \end{aligned} \tag{3}$$

In this embedding the real number a must be chosen so that $a + X(t) > 0$ for all t. We chose $a = 0.5$ and computed the linking numbers of the three orbits. The linking numbers in this embedding were computed by carrying out the Gauss linking number integral numerically. The results are:

Link	1	2	4
1		-5	-10
2	-5		-21
4	-10	-21	

(4)

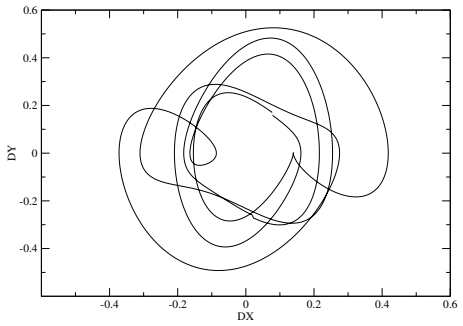

FIG. 6: Projection of the difference $\mathbf{X}_2(t) - \mathbf{X}_1(t)$ onto the X-$\dot{X}$ plane in the intrinsic solid torus $\mathbb{R}^2 \times \mathbb{S}^1$. This difference rotates around the origin 5 times in the clockwise direction. The linking number is -5 and relative rotation rate is $-\frac{5}{2}$.

These are identical to the results obtained in the intrinsic embedding in $\mathbb{R}^2 \times \mathbb{S}^1$. We note here that the choice $X_3(t) = -Y(t)$ instead of $+Y(t)$ simultaneously changes: the parity, that is, the direction of folding from right-handed to left-handed [12, 13]; the global torsion from -3 to $+3$; and the signs of all linking numbers and relative rotation rates.

IV. A FAMILY OF MAPPINGS

A standard procedure for constructing geometry from a scalar time series involves time delay coordinates [1, 2]. Other useful embedding procedures use differential coordinates, Fourier-processed fractional derivatives and integrals, and Hilbert transforms [12].

A three-dimensional time delay embedding can be obtained from the mapping

$$X(i) \to \mathbf{X}(i) = [X(i), X(i-\tau_1), X(i-\tau_2)] \qquad (5)$$

It is customary to choose $\tau_i = i\tau_0$, where τ_0 is some fixed time delay. If τ_0 is very small the embedding is equivalent, under an affine transformation, to a differential embedding [11, 12].

For their study of embeddings, Mindlin and Solari chose τ_1 small and took the second coordinate to be $X_2(i) = X(i) - X(i-k)$, with k small ($k \simeq 5$), so this coordinate is a surrogate for the time derivative of X: $X_2(t) \sim dX/dt = Y(t)$. They allowed the second delay $\tau_2 = \tau$ to vary over a wide range of values. The one-parameter family of embeddings they chose to study was the discretized version of

$$X(t) \to \mathbf{X}(t) = \left[X(t), Y(t) = \frac{dX(t)}{dt}, X(t-\tau)\right] \qquad (6)$$

This one-parameter family of mappings was used to map the strange attractor into $\mathbb{R}^3$. For some values of τ this mapping is not even 1-1 (e.g., $\tau = 0$). For other values the mapping is everywhere a local diffeomorphism but self-intersections occur in the image of the strange attractor. For yet other values of τ the mapping is a global diffeomorphism. In these three cases we call the mapping an:

$$\begin{array}{ccccc} \text{injection} & \to & \text{immersion} & \to & \text{embedding} \\ \text{Not } 1-1 & & \text{Locally } 1-1 & & \text{Globally } 1-1 \end{array}$$

The projection of the strange attractor generated by (1) and mapped into $\mathbb{R}^3$ under (6), onto the X-Y plane is shown in Fig. 1. The projection is independent of the single delay parameter τ. The flow is clockwise.

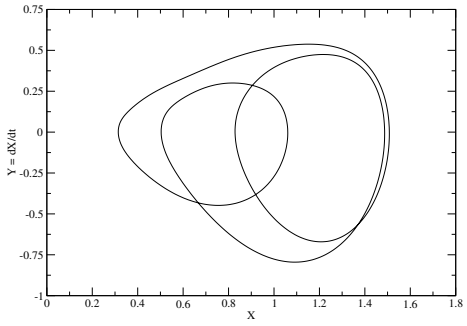

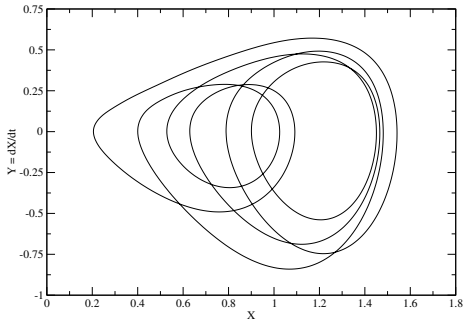

FIG. 7: Period one and two orbits projected onto the X-Y plane. They were obtained by finding surrogate periodic orbits, smoothing in frequency space, and first differencing in the time domain.

The X-Y projections of the period-one and period-two orbits are shown in Fig. 7. These orbits intersect the Poincaré section ϕ = constant in the phase space $\mathbb{R}^2 \times \mathbb{S}^1$ once and twice, respectively. In projection, they can be interpreted either as period-1 and period-2 orbits or as period-3 and period-6 orbits. In fact, they were interpreted as period-3 and period-6 orbits in Ref. [3]. A proper understanding of these orbits is intrinsically

tied to a precise description of the Poincaré section for this dynamical system. The principal difference between the present work and that of Ref. [3] is in the choice of Poincaré section, leading to the interpretation of these orbits as period-1 and period-2 orbits, consistent with the dynamical interpretation of these orbits and the number of intersections of these orbits with the stroboscopic section.

V. CHOICE OF POINCARÉ SECTION

We turn now to the proper choice of a Poincaré section for this dynamical system. We first look at intersections of the strange attractor with the X-Z plane. These intersections occur at $Y = \dot{X} = 0$ and depend on the embedding chosen — that is, on the value of the delay parameter τ. We show intersections with this plane for three different values of τ in Fig. 8. For all values of τ there are six intersections. They occur in the order $A1 \to A2 \to B1 \to B2 \to C1 \to C2 \to A1 \cdots$. At the three intersections $A1$, $B1$, $C1$ to the left of $X[i] = 1$ the flow is into the plane, while at $A2$, $B2$, $C2$ to the right of $X[i] = 1$ it is out of the plane. We have chosen X, Y, Z to be a right-handed coordinate system.

Following standard algorithms of the time, Mindlin and Solari chose the half-plane $Y = 0$, $X > 1$ as a Poincaré section. The two orbits above intersect this half-plane three and six times, leading to their interpretation as period-3 and period-6 orbits. With this choice, the Poincaré section in $\mathbb{R}^3$ and the stroboscopic section in the original phase space $\mathbb{R}^2 \times \mathbb{S}^1$ are inequivalent. Recently a more precise algorithm has been developed for constructing the Poincaré section for chaotic flows in $\mathbb{R}^3$ [7, 8]. Since the developments are so recent, and this point is so important, we briefly review the arguments here.

Strange attractors in $\mathbb{R}^3$ are described and classified by branched manifolds. Branched manifolds in turn can be embedded in three-dimensional manifolds whose bounding surfaces are two-dimensional, closed, bounded, and orientable. Such surfaces have been classified: they are tori of genus g: $g = 0, 1, 2, \cdots$. In fact, branched manifolds can be bounded by tori of genus $g = 1$ or $g \geq 3$ [7, 8]. The torus with genus $g = 1$ is a donut. Its homotopy group has two generators: one longitude and one meridian [16]. The meridian can be chosen to bound a disk that lies entirely inside the region bounded by the surface, and which is at all points transverse to the flow. This disk is a Poincaré section for the flow.

In the case $g \geq 3$ there are g longitudes and g meridians. Each meridian bounds a disk that lies completely inside the bounding torus and that is transverse to the flow. Of these g disks, $g - 1$ provide information about the structure of the flow. They can be taken as $g - 1$ components of the Poincaré section. The Poincaré section is the disjoint union of $g - 1$ disks, each bounded by a meridian in the homotopy group of the genus-g torus [7, 8]. For any branched manifold contained in a bounding torus, at least two branches leave each disk and at least two branches arrive at each disk ($g = 1, g \geq 3$).

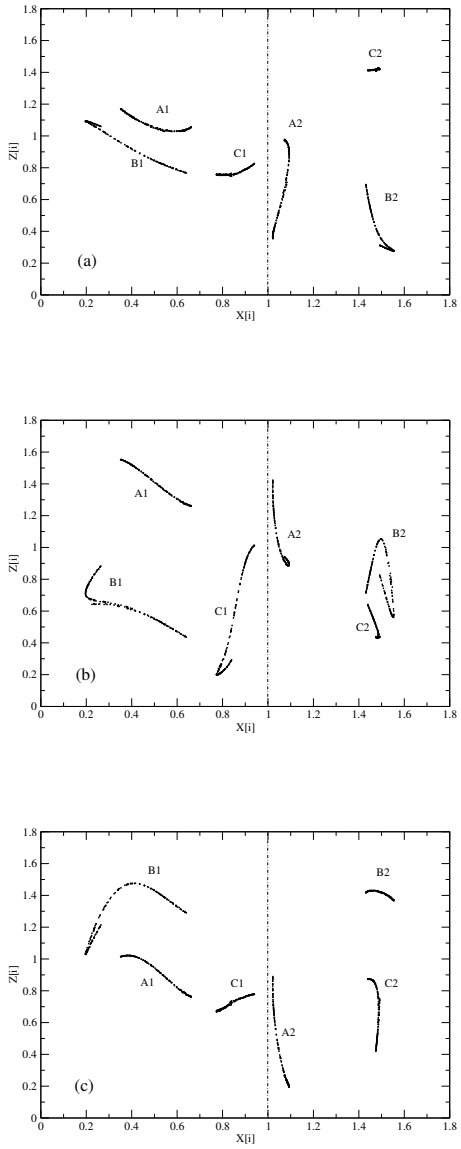

FIG. 8: Intersections of the strange attractor generated by Eq. (1) with the plane $\dot{X} = 0$ under the embedding (6). The intersections occur in the order $A1 \to A2 \to B1 \to B2 \to C1 \to C2 \to A1$. The flow at $A1$, $B1$, and $C1$ is into the plane while the flow at $A2$, $B2$, and $C2$ is out of the plane. (a) $\tau = \frac{225}{1024}T$, (b) $\tau = \frac{425}{1024}T$, (c) $\tau = -\frac{225}{1024}T$.

As with branched manifolds, the flow between the components of the Poincaré section is summarized by a tran-

sition matrix. This is a $(g-1)\times(g-1)$ matrix ($g \geq 3$). The structure of bounding tori places severe constraints on the transition matrix. Initial conditions on any component can flow to only two other components. In other words, the outset from any component flows to exactly two other components. Similarly, the inset to any components arrives from exactly two other components [7, 8]. As a result, for $g \geq 3$ the transition matrix for flows between components of the Poincaré section has two entries $+1$ in each row and in each column.

We now apply this algorithm to choose a Poincaré section for the flow studied in [3]. In any embedding the flow can be embedded in a bounding torus. The intersection of this bounding torus with the half-plane $Y = 0, X > 1$ (Fig. 8) consists of three disks surrounding $A2, B2, C2$. The transition matrix for these disks, under the flow, is a cyclic 3×3 matrix, with one entry 1 in each row and each column. As a result, the bounding torus has genus $g = 1$. As a result, the Poincaré section consists of a single disk transverse to the flow. The disk surrounding $A2$ or $B2$ or $C2$ can be taken as the Poincaré section. Since a global Poincaré section exists there is no problem about constructing braids. In fact, every choice of Poincaré section (i.e, a disk surrounding any one of the six intersections shown in Fig. 8) leads to the same set of braids for any fixed value of τ that provides an embedding.

The set of unstable periodic orbits in a strange attractor is independent of the embedding. This point was forcefully made in [11, 12], where it was pointed out that such orbits can be identified by a close returns analysis on scalar time series *before an embedding is made*. As a result, the strange attractor embedded in the natural phase space $\mathbb{R}^2 \times \mathbb{S}^1$, in the preferred framing of $\mathbb{R}^2 \times \mathbb{S}^1$ in $\mathbb{R}^3$, and the attractors obtained from the map (6) with values of τ that provide embeddings, all have the same spectrum of unstable periodic orbits. For each embedding the spectrum can be described by a finite braid by restricting to a basis set of orbits up to some finite period.

How are the braids in the phase space $\mathbb{R}^2 \times \mathbb{S}^1$, the preferred framing in $\mathbb{R}^3$, and embeddings in $\mathbb{R}^3$ under the one-parameter family (6), related to each other?

VI. EXTRINSIC EMBEDDINGS

Mindlin and Solari found two ranges of τ values at which embeddings existed. They were separated by a range of τ values at which self-intersections occurred. The self-intersections reduced the image of the attractor in $\mathbb{R}^3$ to an immersion (at best) or possibly an injection.

This transition from one range of τ values that provide an embedding to a second range that provide a different embedding can be inferred from Fig. 8(a) and 8(b). In each case the intersections of the image with the $Y = 0$ plane are well-separated. This does not mean that the corresponding τ values provide an embedding - only that they might. As τ changes continuously from $\frac{225}{1024}T$ (Fig 8(a)) to $\frac{425}{1024}T$ (Fig. 8(b)) the intersections $B2$ and $C2$ pass through each other. For some intermediate range of τ values the image attractor must undergo self-intersections. For this range of τ values the mapping is at best an immersion.

The topological structure of the embedded strange attractors for $\tau = \frac{225}{1024}T$ (Fig. 8(a)) and $\tau = \frac{425}{1024}T$ (Fig. 8(b)) were determined by computing linking numbers of some low-period orbits. We found that for $\tau = \frac{225}{1024}T$ the embedded attractor was generated by a right-handed Smale horseshoe mechanism with global torsion -1. For $\tau = \frac{425}{1024}T$ the embedded attractor was generated by a left-handed Smale horseshoe mechanism with global torsion $+1$. The table of linking numbers for one embedding was the negative of the table, for the same orbits, in the other embedding.

We also studied the one-parameter family of mappings for $\tau < 0$: that is, we studied time advance embeddings, with similar results. For $\tau = -\frac{525}{1024}T$ the intersection was qualitatively the same as shown in Fig. 8(b). The intersection for $\tau = -\frac{225}{1024}T$ is shown in Fig. 8(c). In passing from $-\frac{525}{1024}T$ to $-\frac{225}{1024}T$ the intersections labeled $A1$ and $B1$ exchange places. For an intermediate range of τ values the time advance mapping exhibits self-intersections and cannot be an embedding.

The change in global torsion, from -1 to $+1$, can be understood as shown in Fig. 9. In one case the flow spirals up ($B2 \to C1 \to C2$ in Fig. 8(a)), while in the other case the flow spirals down ($B2 \to C1 \to C2$ in Fig. 8(b)). As the torus that cycles three times around is unwound to a torus that cycles only once, a global torsion of ±1 is introduced, depending on the direction of the spiral. This is equivalent to the exchange of writhe for twist in ribbons.

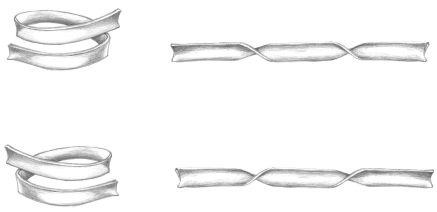

FIG. 9: When the ribbon with writhe but no twist is stretched, twist is induced. The direction of the twist depends on the coil of the ribbon.

The change from right-handed to left-handed folding to generate a horseshoe occurs as the immersion degenerates to an injection. On either side of this degeneracy folding occurs in a different direction. That the parity can change in a one-parameter family of mappings is easily seen from the embeddings given by $x(t) \to$

$(x(t), x(t) + \alpha\dot{x}(t), \ddot{x}(t))$. For $\alpha = 0$ the map is an injection, while embeddings of opposite parity are obtained for α large and positive and negative.

VII. THE SELF-INTERSECTION PROBLEM

It is not an easy problem to identify parameter values at which self-intersections of the immersed attractor occur. This problem was carefully treated by Mindlin and Solari [3]. It is possible to provide a less complete answer to this question by studying a simplified problem. The idea is to embed the strange attractor in a torus and look for self-intersections of the torus. If the torus has no self-intersections the attractor it contains certainly has no self-intersections. However, the converse is not true: the torus my have self-intersections while the strange attractor has none.

The problem can be simplified even further by using the period-one orbit in the attractor as a guiding curve for the torus. It is then a simple matter to search for self-intersections of this curve. Generically, a closed curve mapped into $\mathbb{R}^3$ has no self-intersections. However, we are looking for self-intersections in a one-parameter *family* of circles mapped into $\mathbb{R}^3$, and these generically occur in zero dimensional sets (isolated points). When the guiding curve has self-intersections, the torus surrounding it has self-intersections and the strange attractor in which this curve is embedded also has self-intersections. Values of τ at which self intersections occur are surrounded by open sets in which the map (6) is not an embedding. Once again this simple search does not completely answer the self-intersection question: we cannot show that if self intersections of the guiding period one orbit occur at τ_1 and at τ_3 ($\tau_1 < \tau_3$) there is some intermediate value τ_2, $\tau_1 < \tau_2 < \tau_3$, that provides an embedding for the strange attractor.

To locate self-intersections of the period-one orbit in the strange attractor, we show its X-Y projection in Fig. 10. In this projection there are four self-intersections, labeled $a,\ b,\ c,\ d$ in the order in which they are encountered following the trajectory starting at the arrow. At each intersection we show the tangent vectors to the two segments that cross. The usual convention is adopted: the crossing is positive if the upper tangent (larger Z value) can be rotated into the lower tangent vector using the right hand. At each of the four points $a,\ b,\ c,\ d$ we computed the height difference (ΔZ) in such a way that if the difference is positive the crossing is right-handed, and therefore positive. This was done for all values of the delay τ. Since the guiding curve is a period-one orbit, only delays up to one forcing period need be considered. Since FFT processing was used, a delay of $1024 = 2^{10}$ corresponds to T. The results are shown for the four points $a,\ b,\ c,\ d$ in Fig. 11. This figure shows, for example, that at a delay $\tau = \frac{1}{2}T$ the crossings at $a,\ b$ and d are positive while that at c is negative. In addition to the four zero crossings that can occur for the injection at $\tau = 0$ there are 12 isolated zero crossings for nonzero values of the delay.

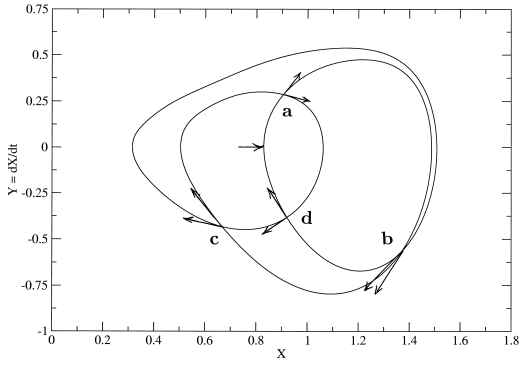

FIG. 10: Tangent vectors are drawn to the segments at each of the four crossing points, reached in the order $a,\ b,\ c,\ d$ starting from the arrow.

Only one knot has four crossings in projection: this is the figure 8 knot. Therefore any of the embeddings of the period-one orbit into $\mathbb{R}^3$ is either unknotted or equivalent to the figure 8 knot. Of 2^4 possible embeddings suggested by Fig. 10, 12 are unknotted and four are knotted. The embeddings knotted like the figure 8 knot have crossings at (a, b, c, d) given by $(+,+,+,+)$, $(-,-,-,-)$, $(+,-,-,+)$, and $(-,+,+,-)$. The succession of crossings, starting at the arrow, are *uuoouuoo*, *oouuoouu*, *uouououo*, and *ouououou* (resp.), where *o* is an overcrossing and *u* is an undercrossing. From Fig. 11 we can see that there is no value of τ for which the embedding of the period-one orbit in $\mathbb{R}^3$ is knotted.

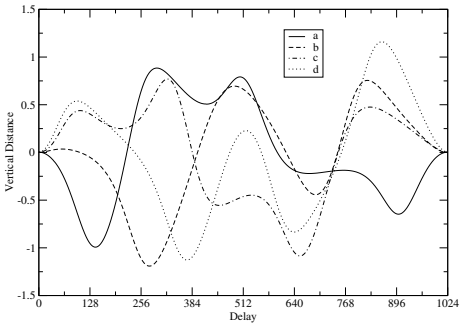

FIG. 11: Vertical distance between the orbit segments at the four points $a,\ b,\ c,\ d$. These are points of apparent self-intersection when projected to the $X, \dot{X}$ plane. Real self-intersections occur in $\mathbb{R}^3$ when the vertical offset is zero.

We conclude from Figs. 9-11 that several different values of τ provide embeddings of the strange attractor in $\mathbb{R}^2 \times \mathbb{S}^1$ into $\mathbb{R}^3$. These values are separated by values of τ for which the immersed attractor has self-intersections. When an embedding exists, the period-one orbit in the flow is unknotted. The solid torus for which it is the guiding knot is also unknotted. However, the solid torus is three dimensional while the period-one orbit is one-dimensional. Although different embeddings of an unknot in $\mathbb{R}^3$ can be isotoped to each other, the same is not true of the three-dimensional tori surrounding these unknots, as can be seen in Fig. 9 (left-hand side).

The embedding strange attractors that we have studied all describe a Smale horseshoe mechanism for generating chaos. The embeddings differ from each other in handedness (parity) and global torsion. There is also the possibility, not realized in the class of embeddings studied here and in [3], that the knot type of the bounding torus containing the strange attractor can change as the parameter values change. The topological properties of a strange attractor are in part embedding-dependent. We believe that the only ways embeddings can differ from each other, and from the underlying dynamics are: the handedness of the folding; the global torsion; and the knot type of the period-one orbit. We believe embeddings preserve mechanism - that is, the template matrices and layering information, up to sign and global torsion.

VIII. SUMMARY AND CONCLUSIONS

The purpose of [3] was to raise a red flag on the black-box-like application of topological tools to analyze data. In particular, the usual standard choice for a Poincaré section - a half-plane - lead to subtleties in the construction and interpretation of braids. Mindlin and Solari traced these difficulties to non-overlapping intersections of the embedded strange attractor with the half-plane chosen as the Poincaré section. They also pointed out that the topological structure of a chaotic flow is embedding dependent. With their choice of Poincaré section they identified an orbit of period three that had zero topological entropy in one embedding and positive topological entropy in another. This violates a basic theorem: topological entropy is embedding independent [6].

The purpose of the present work is to show that the topological analysis of strange attractors is robust against changes in the embedding. Key to this robustness is the proper choice of a global Poincaré section. This is possible due to recent advances in our understanding of the structure of chaos in low dimensions [7, 8]. Specifically, we applied the algorithm for constructing a global Poincaré section to the embeddings described above. We find that the orbit identified in [3] as a period three orbit is actually the period-one node of the standard Smale horseshoe. There is no difference between the Poincaré section we construct for embeddings in $\mathbb{R}^3$ and the constant phase plane $\phi =$const. in the original phase space $\mathbb{R}^2 \times \mathbb{S}^1$. With this proper choice of Poincaré section, all braids are well-defined and similar from one embedding to another. They differ from each other in a limited number of ways. Specifically, their organization is identical up to mirror image (handedness, or parity), global torsion, and knot type of the embedding in $\mathbb{R}^3$, although all embeddings studied in this work turn out to be unknotted. We believe that embeddings of strange attractors in $\mathbb{R}^3$ can differ from each other in only these three ways.

We believe our findings in the present work are general: the topological structure of a chaotic flow is embedding dependent (by parity, global torsion, knot or braid type), but the mechanism that generates chaotic behavior (horseshoe in the present case) is the same in every embedding: it is an embedding invariant. Work to verify this assertion is currently under way.

We wish to thank M. Lefranc for verifying the branched manifold for the driven system (1) using 30 periodic orbits. We wish to thank G. B. Mindlin, H. G. Solari, M. Lefranc, and C. Letellier for their interest in this work and for useful comments. This work is partially supported by NSF Grant PHY 9987468.

REFERENCES

[1] N. H. Packard, J. P. Crutchfield, J. D. Farmer, and R. S. Shaw, Phys. Rev. Lett. **45**, 712 (1980).

[2] F. Takens, *Detecting Strange Attractors in Turbulence*, Lecture Notes in Mathematics, Vol. **898**, Berlin: Springer-Verlag, 1981.

[3] G. B. Mindlin and H. G. Solari, Phys. Rev. **E52**(2), 1497 (1995).

[4] T. Ondarcuhu, G. B. Mindlin, H. L. Mancini, and C. Perez-Garcia, Phys. Rev. Lett. **70**, 3892 (1993).

[5] M. Huerta, D. Krmpotic, G. B. Mindlin, H. Mancini, D. Mazza, and C. Perez-Garcia, Physica **D96**(1-4), 200 (1996).

[6] R. L. Adler, A. G. Konheim, and M. H. McAndrew, Trans. Am. Math. Soc. **114**(2), 309-319 (1965).

[7] T. D. Tsankov and R. Gilmore, Phys. Rev. Lett. **91**(13), 134104 (2003).

[8] T. D. Tsankov and R. Gilmore, Topological aspects of the structure of chaotic attractors in $\mathbb{R}^3$, (unpublished).

[9] J. Birman and R. F. Williams, Cont. Math. **20**, 1 (1983).

[10] G. B. Mindlin, H. G. Solari, M. A. Natiello, R. Gilmore, and X.-J. Hou, J. Nonlin. Sci. **1**, 147 (1991).

[11] R. Gilmore, Revs. Mod. Phys. **70**(4), 1455 (1998).

[12] R. Gilmore and M. Lefranc, *The Topology of Chaos*, NY: Wiley, 2002.

[13] H. G. Solari and R. Gilmore, Phys. Rev. **A37**, 3096 (1988).

[14] G. B. Mindlin, R. Lopez-Ruiz, H. G. Solari, and R. Gilmore, Phys. Rev. **E48**, 4297 (1993).
[15] T. Hall, Phys. Rev. Lett. **71**(1), 58 (1993).
[16] D. Rolfsen, *Knots and Links*, (Publish or Perish, Berkeley, 1976).